SUPPORTING INFORMATION for

Energy Conversion via Metal Nanolayers

Mavis D. Boamah,[$] Emilie H. Lozier,[$] Jeongmin Kim,[#] Paul E. Ohno,[$] Catherine E. Walker,[$] Thomas F. Miller III,[#] and Franz M. Geiger[$,*]

[$]Department of Chemistry, Northwestern University, Evanston, IL 60208, USA and

[#]Department of Chemistry, California Institute of Technology, Pasadena, CA, 91125, USA

*Corresponding author: geigerf@chem.northwestern.edu

This document contains data referenced in the main manuscript text.

Supplementary Note 1. Additional Experiments and Controls.

Fig. S1. (**top**) Photograph of 3x9 and 1x3 in^2 glass slide. (**middle**) Cross section of flow cell for 3 x 9 slides. Wetted part in light blue shows vertical flow inlet through the Kalrez monolith (a) and a horizontal flow channel in contact with the metal nanolayer-containing glass slide (b) sandwiched between two silicone sheets (grey) underneath a top slide made from Plexiglas (c). (**bottom**) Photographs of the small flow cell used for the 3 x 1 slides.

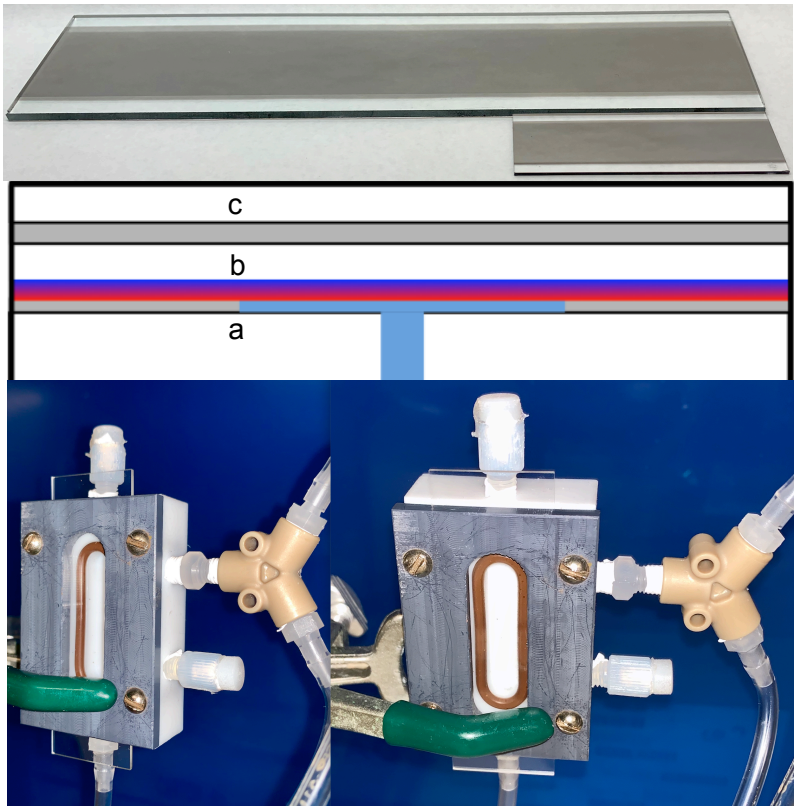

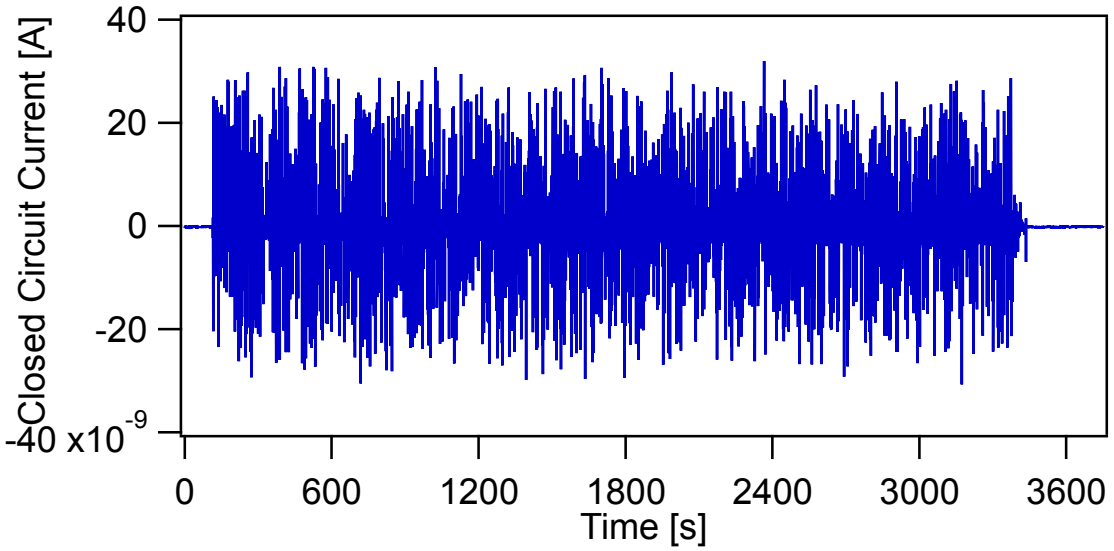

Fig. S2. Closed circuit current for a 10 nm thin iron nanolayer under flow of 600 mM NaCl at pH 8.0 lasting 2 seconds alternating with air flow lasting 2 seconds at a flow rate of 28 mL min^{-1}.

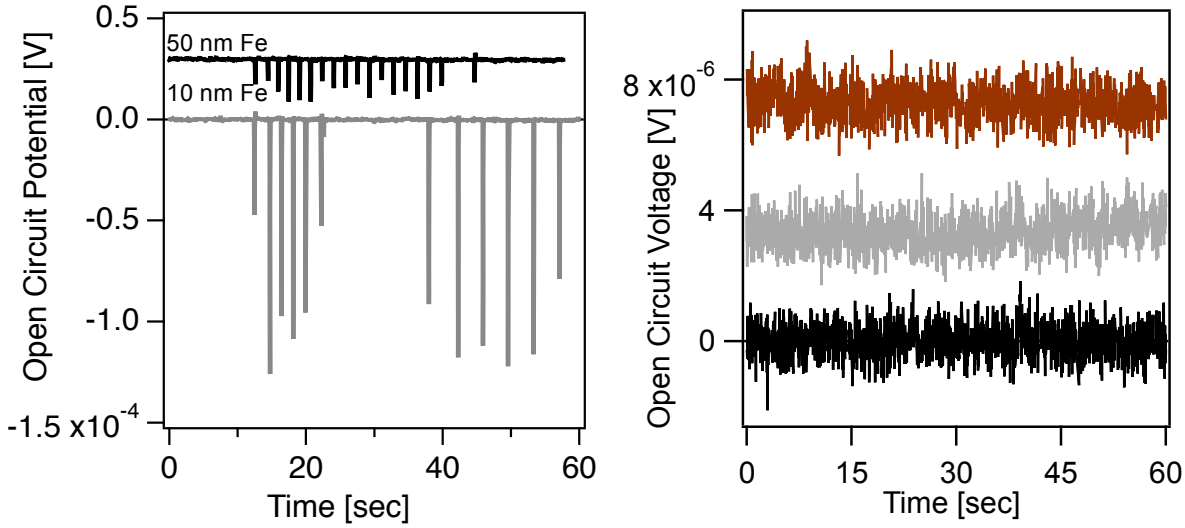

Fig. S3. (**left**), Voltage induced in a 50 nm (black trace) and 10 nm (gray trace) thin iron nanofilm (data offset for clarity); 15 μL drops at a drop rate of 0.5 mL min^{-1}. (**right**) Voltage induced in a 2 mm thick iron plate (black trace), commercial aluminum foil (gray trace, data offset for clarity), and aluminum film inside a snack bag (brown trace, data offset for clarity). 15 μL drops at a drop rate of 0.5 mL min^{-1}.

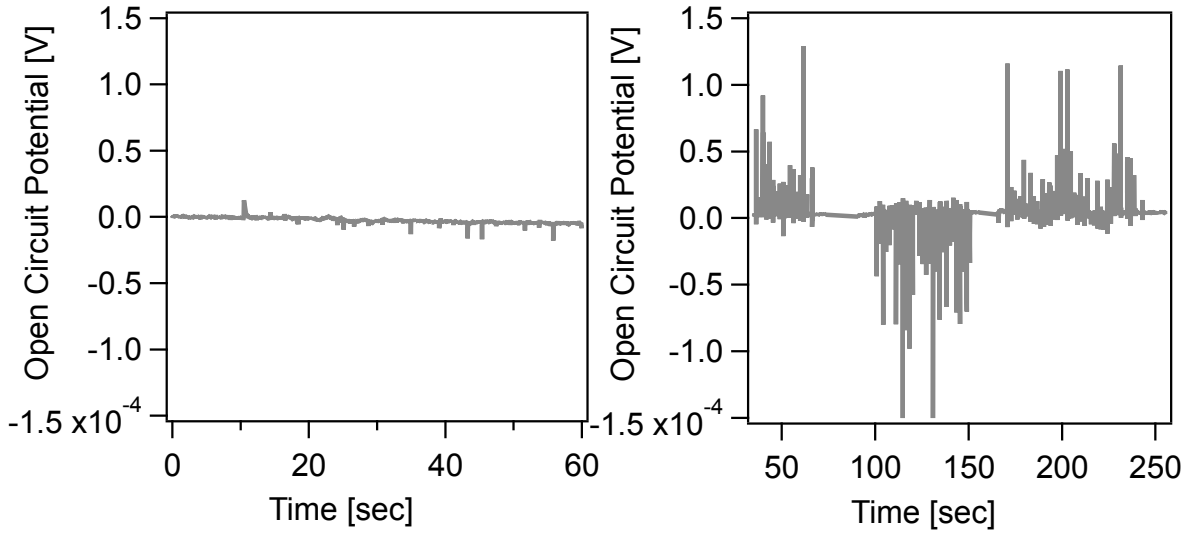

Fig. S4. (**left**) OCV measured perpendicular to the drop motion while dropping a 0.6 M aqueous salt solution (pH 5.8) over a 5 nm thin iron nanofilm at a drop rate=0.5 mL/min and (**right**) when reversing the polarity of the probes.

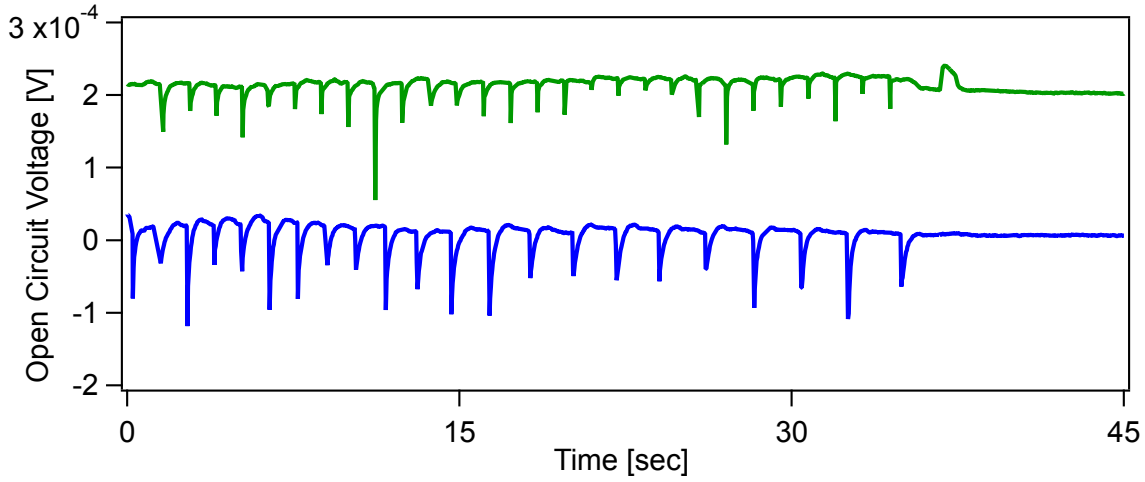

Fig. S5. OCV for a 10 nm thick iron nanofilm using 600 mM salt (top, pH 5.8, offset by 0.2 mV for clarity) and Instant Ocean (bottom, pH 8.3) (drop rate= 0.5 mL min^{-1}).

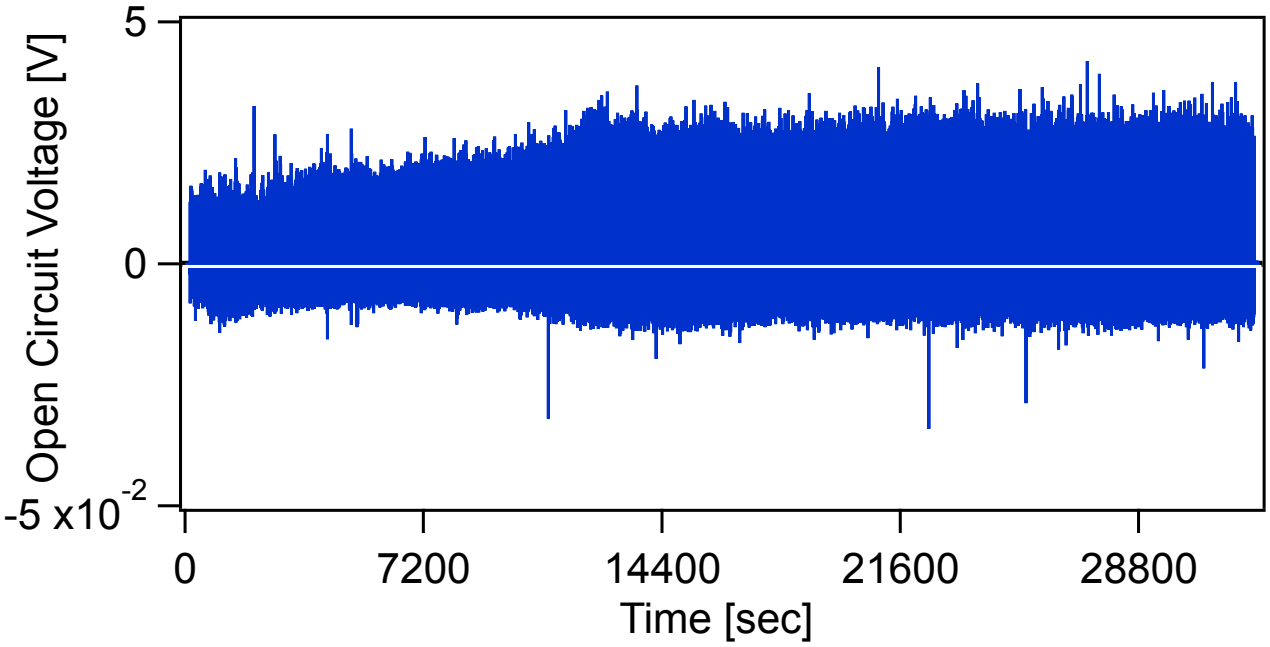

Fig. S6. OCV for a 10 nm thick iron nanofilm using drops alternating between 0.2 mM NaCl at pH 5.8 and 600 mM NaCl at pH 8.0 with a drop rate of 0.5 mL min^{-1}.

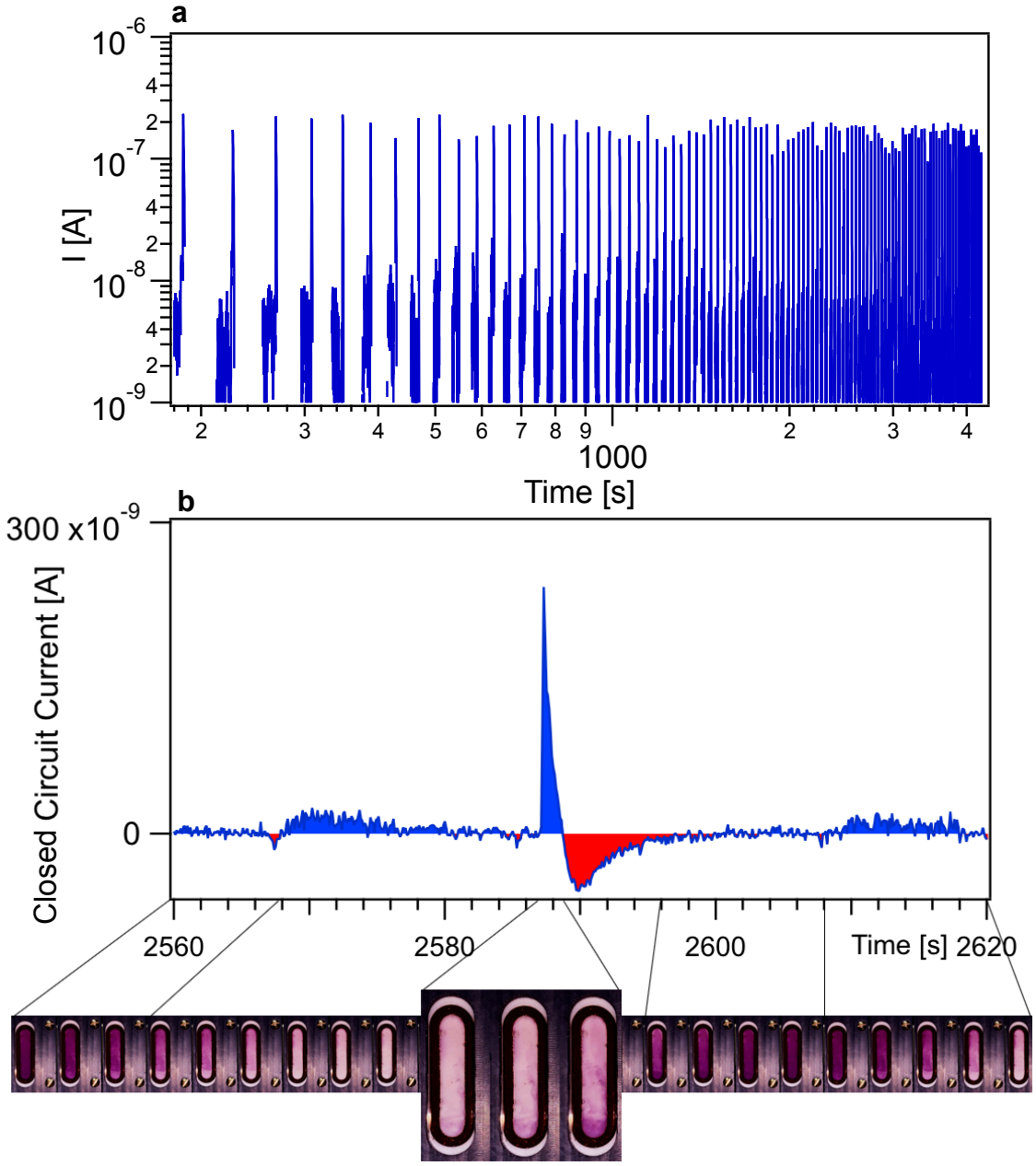

Fig. S7. a, Induced current in a 10 nm iron nanofilm using aqueous solutions of alternating salinity (0.1M and deionized water, 25 mL min^{-1}, 20 sec flow per salinity) over ~1 hour. **b**, Induced current before, during, and after low (deep purple)-to-high (light purple) salinity transition in flow cell and video frames showing turbulent mixing in flow cell during salinity alternation.

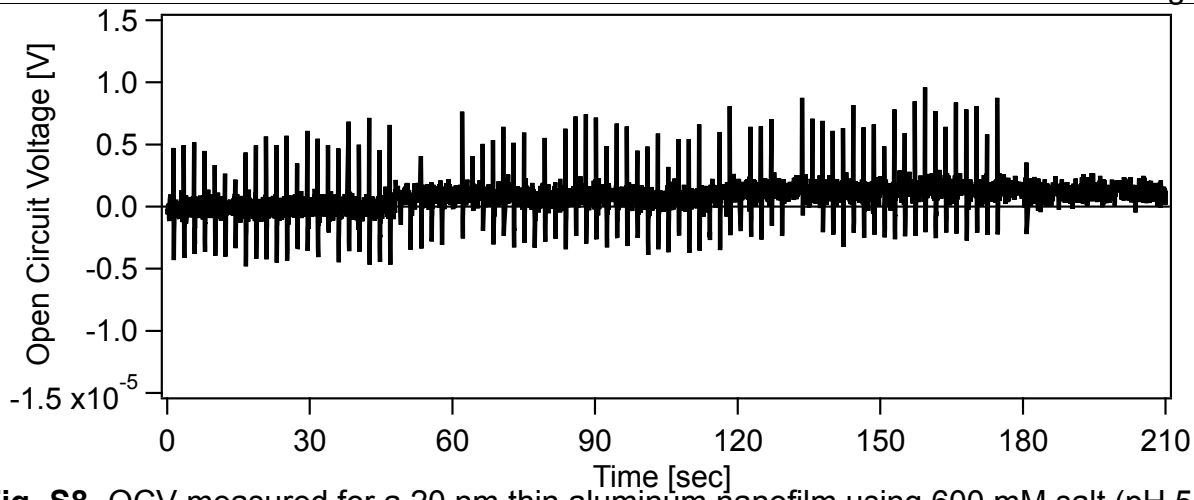

Fig. S8. OCV measured for a 20 nm thin aluminum nanofilm using 600 mM salt (pH 5.8) and a drop rate of 0.5 mL/min.

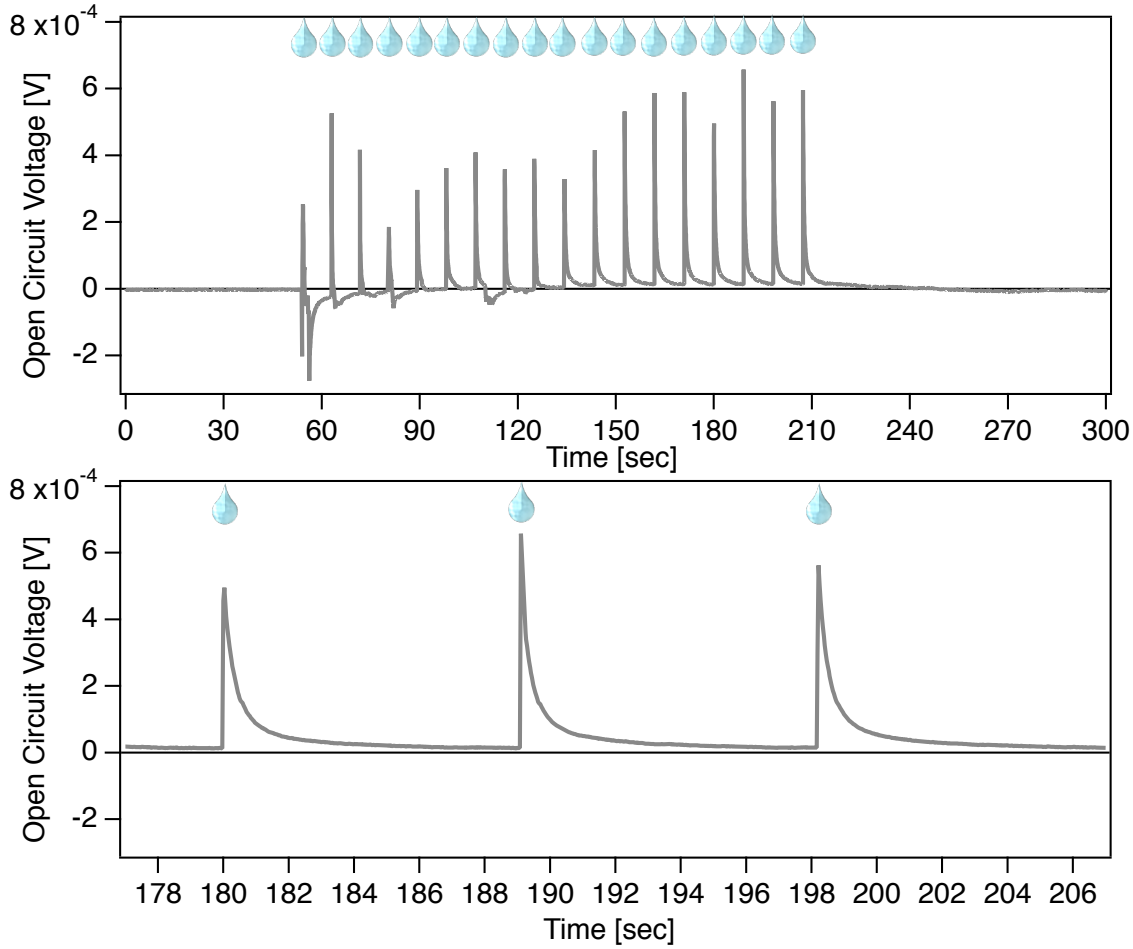

Fig. S9. OCV measured for a freshly prepared 10 nm thin iron nanofilm using 100 mM salt and a drop rate of 0.5 mL/min (top) and zoomed in to show three voltage spike events (bottom).

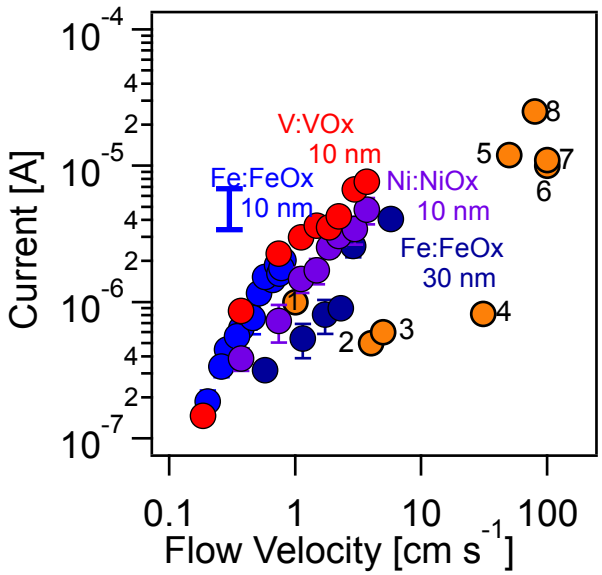

Fig. S10. Plot of Fig. 3b including references provided for the comparison to previously reported results (orange filled circles).1= A. T. Liu *et al.*, Direct Electricity Generation Mediated by Molecular Interactions with Low Dimensional Carbon Materials—A Mechanistic Perspective. *Advanced Energy Materials* **8**, 1 802212 (2018); 2= H. Zhong *et al.*, Two dimensional graphene nanogenerator by coulomb dragging: Moving van der Waals heterostructure. *Applied Physics Letters* **106**, 243903 (2015); 3= J. Park *et al.*, Identification of Droplet-Flow-Induced Electric Energy on Electrolyte–Insulator–Semiconductor Structure. *Journal of the American Chemical Society* **139**, 10968-10971 (2017); 4= Q. Tang, X. Wang, P. Yang, B. He, A Solar Cell That Is Triggered by Sun and Rain. *Angewandte Chemie International Edition* **55**, 5243-5246 (2016); 5= G. Zhu *et al.*, Harvesting Water Wave Energy by Asymmetric Screening of Electrostatic Charges on a Nanostructured Hydrophobic Thin-Film Surface. *ACS Nano* **8**, 6031-6037 (2014); 6= S. Yang *et al.*, Mechanism of Electric Power Generation from Ionic Droplet Motion on Polymer Supported Graphene. *Journal of the American Chemical Society* **140**, 13746-

13752 (2018); 7=. Yin *et al.*, Waving potential in graphene. *Nature Communications* **5**, 3582 (2014); 8= W. Huang *et al.*, Power generation from water flowing through three-dimensional graphene foam. *Nanoscale* **6**, 3921-3924 (2014). These references are also available in the References list below (1-8).

X-ray Photoelectron Spectroscopy (XPS). XPS depth profile measurements were carried out with a Thermo Scientific ESCALAB 250 Xii instrument stationed at the NUANCE center at Northwestern University. The instrument is calibrated to the Au $4f_{7/2}$ line at 83.96 eV. It uses a Kα radiation from a monochromatic aluminum source. A flood gun is used for the ejection of low energy Ar^+ ions and electrons to compensate for surface charging. We employ the 2 mm raster size 2 keV etching mode ion (Ar^+) gun at mid current to prevent the reduction of trivalent ions to divalent ions (9).

The results are shown in Fig. S11. The physical-vapor deposited aluminum nanolayers shows Al(III) species in the oxide nano-overlayer, and the bulk is Al(0)(10, 11). For chromium nanolayers, XPS peaks indicate the presence of Cr(III) oxides in the oxide overlayer and the bulk is Cr(0).(12, 13) We have characterized iron nanolayers with Raman spectroscopy, X-ray diffraction, atom probe tomography, and XPS in our recent publications (14, 15). Iron nanolayers have nano-overlayers containing magnetite and hematite, protecting the Fe(0) bulk. XPS peaks of nickel nanolayers indicate the presence of both Ni(III) and Ni(II) oxides on the surface, while the bulk is Ni(0) (12, 16). For vanadium, we find V(V)/(IV) oxides on the surface, while the bulk is V(0). (12, 17)

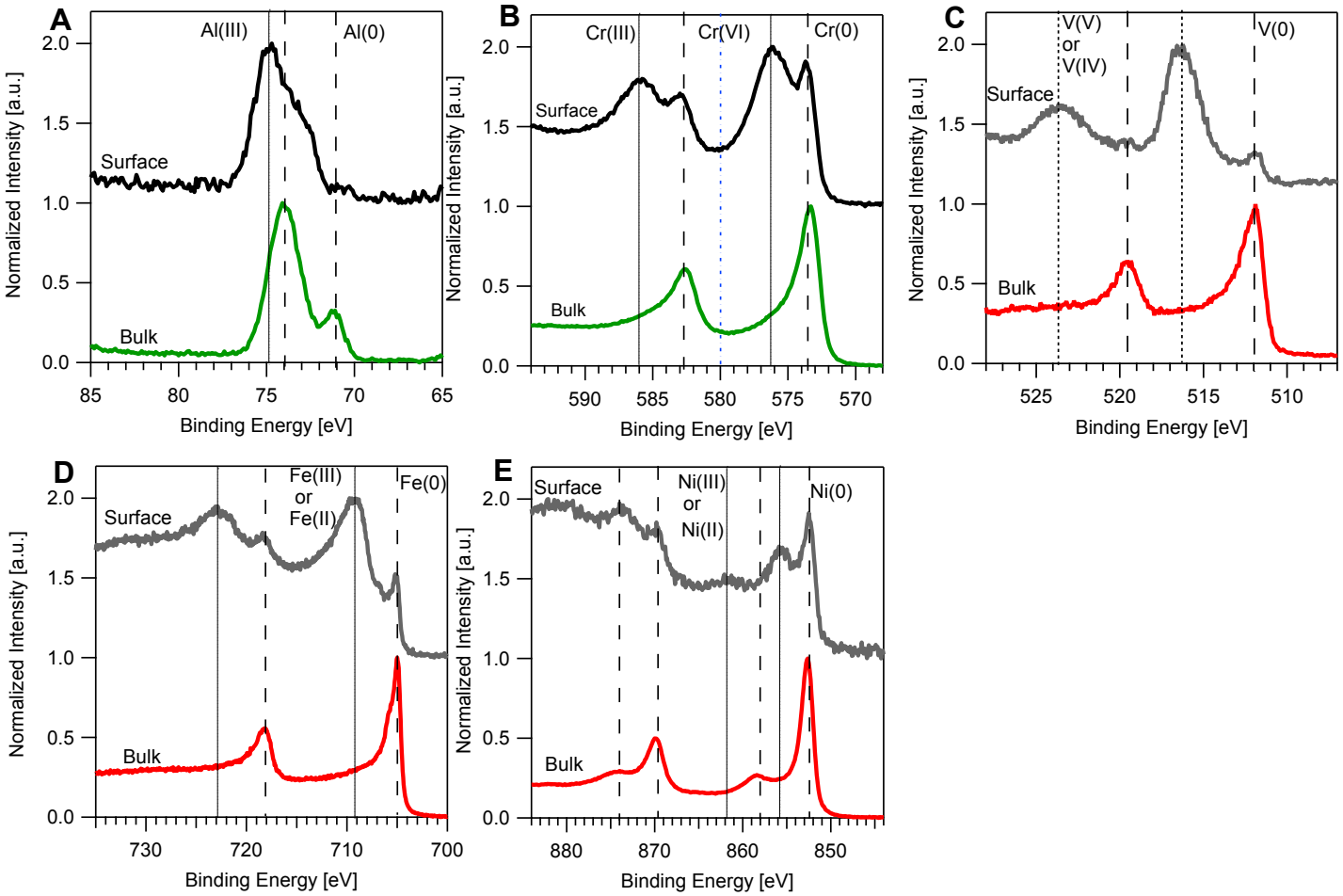

Figure S11. XPS depth profile graphs of ~10 nm (A) Al:AlOx, (B) Cr:CrOx, (C) Fe:FeOx, and (D) Ni:NiOx films deposited on microscope slides. Big and small black dashed lines represent peaks for zero-valent and trivalent/divalent forms of the elements identified, respectively. Blue dashed vertical line in (B) shows the absence of hexavalent chromium [Cr(VI)] peaks in the CrOx nano-overlayer. Vertical dotted lines in (C) show the presence of V(IV) and V(V) in the VOx nano-overlayers, while the dashed lines show V(0). Vertical solid lines in (D) and (E) show the presence of M(II) and M(III) in the FeOx and NiOx nano-overlayers. Please see text for details.

Supplementary Note 2. Computational methods. Molecular dynamics simulations are performed using a polarizable model for the conductive regions of the iron nanolayer. In

these simulations, we do not account for possible redox activity in the oxide layer, instead simply modeling it as an insulator. The atoms in the nanolayer are fixed in the face-centered cubic structure with a lattice parameter of 0.392 nm and a (111) termination at the interface. The orthorhombic simulation cell is oriented such that the *z* coordinate is perpendicular to the nanolayer surface, and the *x* coordinate coincides with the direction of the gate motion, and the simulation cell is periodically replicated only in the *x* and *y* coordinates. In all simulations, the length of the simulation cell in the *x* and *y* coordinates is 4.979 nm and 4.791 nm, respectively, such that the nanolayer is described using seven layers of atoms, with each nanolayer layer containing 360 atoms (for a total of 2520 nanolayer atoms). Atoms in the nanolayer are modeled as being either oxide-like (i.e., non-polarizable) or metallic (i.e., perfectly conductive). In all simulations, the top layer of atoms in the nanolayer is assumed to be oxide-like, and the arrangement of oxide-like atoms below the nanolayer surface is varied to model the subsurface heterostructure, as described.

Interactions between atoms in the nanolayer and other atoms in the simulation cell are described using both electrostatic and Lennard-Jones (LJ) interactions. Oxide-like atoms in the nanolayer are uncharged, while the charges of the metallic atoms of the nanolayer are allowed to fluctuate in response to charges in the solution. The metallic portion of the nanolayer is modeled as one of two fixed-potential electrodes with zero potential bias, with the fluctuating charge distribution in the metallic portion of the nanolayer described in terms of a sum of atom-centered spherical Gaussian functions,

$$Q_i(\boldsymbol{r}, t) = A_i(t) * \left(\frac{\eta^2}{\pi}\right)^{3/2} exp[-\eta^2(\boldsymbol{r} - \boldsymbol{R}_i)], \qquad \text{Eqn. S1}$$

of width η=19.79 nm^{-1} and amplitude $A_i(t)$ that is determined using an extended Lagrangian method (18). Although all calculations involving the iron nanolayer focus on a single solid/liquid interface, the fixed-potential electrode simulation model requires that two electrodes be included in the simulation cell; the second polarizable electrode was simply placed a large distance from the interface of interest, separated by ~10 nm of vacuum in the *z* coordinate. All simulations are performed using the LAMMPS software package (19).

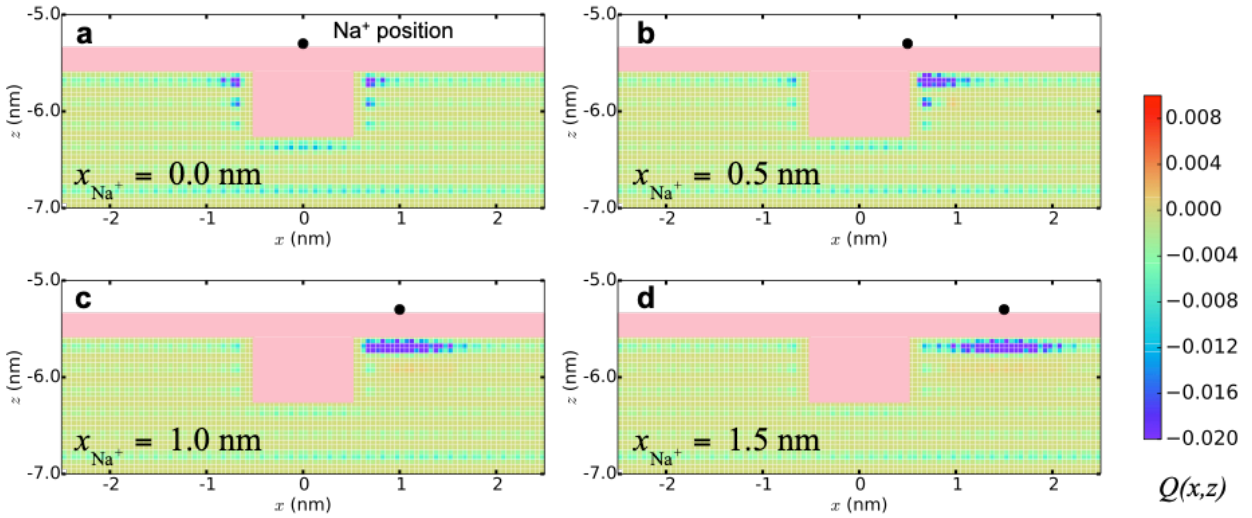

Fig. S12. For various positions of a single monocation, the distribution of induced charge in the metallic portion of the nanolayer, *Q*(*x*,*z*), integrated over the *y*-coordinate of the simulation cell. Nonpolarizable oxide atoms are indicated in pink. The position of the monocation is indicated with the black circle, illustrating various displacements with respect to the position of the subsurface heterostructure.

Nanolayer/liquid interface MD simulations. Simulations of aqueous solutions in contact with the nanolayer were performed using SPC/E water and NaCl ions (20, 21). LJ parameters for the Na+, Cl-, and nanolayer atoms are provided in Table S1. The

cross terms are obtained using Lorentz-Berthelot mixing rule. The LJ interactions and the real-space part of the Coulomb interactions are truncated at 0.98 nm; the long-range contribution of Coulomb interaction is treated by the particle-particle particle-mesh method (22). Via these LJ interactions, the oxide surface preferentially interacts with the Na^+ cations over the Cl^- anions.

	σ (nm)	ε (kcal/mol)
Na^+	0.235	0.13
Cl^-	0.44	0.1
O (SPC/E water)	0.3166	0.1554
Nanolayer atom	0.2534	0.078

Table S1. Lennard-Jones parameters for water, ions, and nanolayer atom (23).

To enforce the regions of alternating salinity in the solution (Fig. 4e), semipermeable boundaries are introduced to interact only with the NaCl ions; the boundaries are positioned at x=1.25 nm and x=-1.25 nm in the simulation cell, and they interact only with the salt ions via a truncated LJ potential with epsilon=10 kcal/mol and sigma=cutoff=0.1 nm. Simulations of the solution/nanolayer were initialized with a slab of water/ions in contact with the nanolayer; after a short period of equilibration, the outermost layer (furthest from the nanolayer) was frozen in space to provide a fixed, amorphous boundary between the solution region and the vacuum of the remaining simulation cell. Finally, the distance between this fixed layer of water molecules and the position of the nanolayer was adjusted so that the pressure of the confined solution was 1 atm, and it was confirmed that the osmotic pressure introduced by the semipermeable

boundaries did not significantly alter the density of water in the ionized vs. deionized solution regions. The final thickness of water along the confinement is ~ 3 nm.

The classical molecular dynamics equations of motion were evolved using the velocity Verlet integrator with a timestep of 2 fs; rigid-body constraints for the water molecules were enforced using the SHAKE algorithm (24). The simulations were performed at a temperature of 298.15 K, enforced via the Nosé-Hoover thermostat with a damping timescale of 100 timesteps.

Supplementary Note 3. Fig. S13 presents the equivalent circuit for the current induced in the system of liquid flow across the nanolayer with alternating high- and low-salinity segments. The leftward electrical current in the nanofilm is generated by the relative motion of the ions (adsorption or desorption) that form the electrical double layer as the salinity gradient boundaries move.

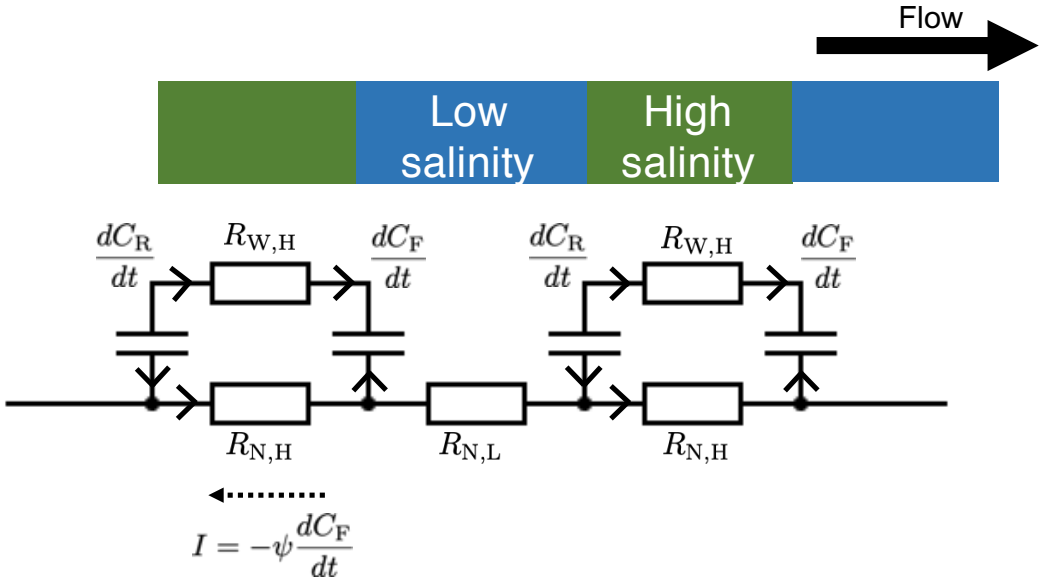

Fig. S13. Equivalent circuit for the current induced in the system of liquid flow across the nanolayer with alternating high- and low-salinity segments. At top, the alternating salinity of the liquid and flow direction are indicated. The liquid resistance to ion flow at

low and high salinity are indicated by $R_{W,L}$ and $R_{W,H}$, respectively. The resistance to electron flow in the contact area between the nanolayer and water at low and high salinity are indicated by $R_{N,L}$ and $R_{N,H}$, respectively. The interfacial capacitance at the front and rear salinity boundaries (C_F and C_R, respectively), which include contributions from the redox activity of the semiconducting metal oxide layer.

Note that **Fig. S13** is closely related to the equivalent circuit presented for droplet motion on graphene in Ref. 2 of the main text (25), with two key distinctions. First, the current case is for liquid flow with alternating salinity. Second (and more important), the interfacial capacitance in the system presented here includes contributions from both the image charge formation in the metal layer as well as the large effect of electron transfer within the semiconducting metal oxide layer of the nanofilm surfaces.

Supplementary Note 4. PVD onto solid and flexible polymers.

Fig. S14. Current density vs flow velocity for a ca. 35 nm thin Fe:FeOx nanmolayer on a poly(ethylene) terephthalate (PET) substrate obtained when alternating deionized water and 1 M NaCl solution segments every 20 sec.

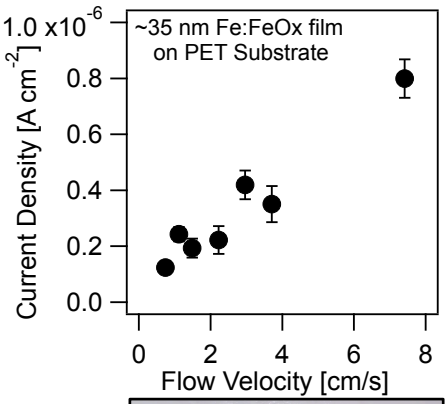

Fig. S15. Photograph of Fe:FeOx nanolayer PVD's onto Saran wrap glued to two wooden handles.

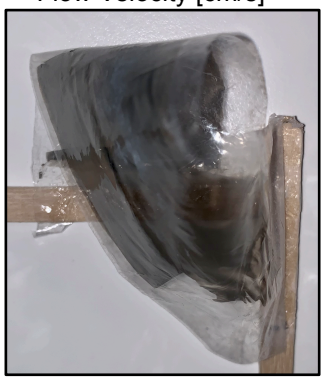

References

1. A. T. Liu *et al.*, Direct Electricity Generation Mediated by Molecular Interactions with Low Dimensional Carbon Materials—A Mechanistic Perspective. *Adv. Energy Mat.* **8**, 1802212 (2018).
2. H. Zhong *et al.*, Two dimensional graphene nanogenerator by coulomb dragging: Moving van der Waals heterostructure. *Appl. Phys. Lett.* **106**, 243903 (2015).
3. J. Park *et al.*, Identification of Droplet-Flow-Induced Electric Energy on Electrolyte−Insulator−Semiconductor Structure. *J. Am. Chem. Soc.* **139**, 10968-10971 (2017).
4. Q. Tang, W. Wang, P. Yang, B. He, A Solar Cell That Is Triggered by Sun and Rain. *Angew. Chem. Int. Ed.* **55** (2016).
5. G. Zhu *et al.*, Harvesting Water Wave Energy by Asymmetric Screening of Electrostatic Charges on a Nanostructured Hydrophobic Thin-Film Surface. *ACS Nano* **8** (2014).
6. S. Yang *et al.*, Mechanism of Electric Power Generation from Ionic Droplet Motion on Polymer Supported Graphene. *J. Am. Chem. Soc.* **140** (2018).
7. J. Yin *et al.*, Waving potential in graphene. *Nature communications* **5** (2014).
8. W. Huang *et al.*, Power generation from water flowing through three-dimensional graphene foam. *Nanoscale* **6**, 3921-3924 (2013).
9. L. I. Yin, S. Ghose, I. Adler, X-ray Photoelectron Spectroscopic Studies of Valence States Produced by Ion-Sputtering Reduction. *Appl. Spectrosc.* **26**, 355-357 (1972).
10. F. Cordier, E. Ollivier, X-ray photoelectron spectroscopy study of aluminium surfaces prepared by anodizing processes. **23**, 601-608 (1995).
11. D. Kaplowitz, G. Jian, K. Gaskell, R. Jacob, M. R.Zachariah, *Synthesis and Reactive Properties of Iron Oxide Coated Nanoaluminum* (2013), vol. 32, pp. 94-104.
12. D. Briggs, Handbook of X-ray Photoelectron Spectroscopy C. D. Wanger, W. M. Riggs, L. E. Davis, J. F. Moulder and G. E.Muilenberg Perkin-Elmer Corp., Physical Electronics Division, Eden Prairie, Minnesota, USA, 1979. 190 pp. $195. **3**, v-v (1981).
13. A. M. Salvi, J. E. Castle, J. F. Watts, E. Desimoni, Peak fitting of the chromium 2p XPS spectrum. *Applied Surface Science* **90**, 333-341 (1995).
14. M. D. Boamah, D. Isheim, F. M. Geiger, Dendritic Oxide Growth in Zerovalent Iron Nanofilms Revealed by Atom Probe Tomography. *The Journal of Physical Chemistry C* **122**, 28225-28232 (2018).
15. D. Faurie-Wisniewski, F. M. Geiger, Synthesis and Characterization of Chemically Pure Nanometer-Thin Zero-Valent Iron Films and Their Surfaces. *The Journal of Physical Chemistry C* **118**, 23256-23263 (2014).
16. A. P. Grosvenor, M. C. Biesinger, R. S. C. Smart, N. S. McIntyre, New interpretations of XPS spectra of nickel metal and oxides. *Surface Science* **600**, 1771-1779 (2006).
17. G. Silversmit, D. Delpa, H. Poelman, G. B. Marin, R. De Gryse, Determination of the V2p XPS binding energies for different vanadium oxidation states (V5+ to V0+). *J. Electron Spectros. Relat. Phenomena* **135**, 167-175 (2004).
18. J. I. Siepmann, M. Sprik, Influence of surface topology and electrostatic potential on water/electrode systems. *J. Chem. Phys.* **102** (1995).
19. S. Plimpton, Fast Parallel Algorithms for Short-Range Molecular Dynamics. *J. Comp. Phys.* **117**, 1-19 (1995).
20. H. J. C. Berendsen, J. R. Grigera, T. P. Straastsma, The Missing Term in Effective Pair Potentials. *J. Phys. Chem.* **91** (1987).
21. D. E. Smith, X. L. Dang, Computer simulations of NaCl association in polarizable water. *J. Chem. Phys.* **100** (1994).
22. R. W. Hockney, J. W. Eastwood, *Computer Simulation Using Particles* (Raylor & Francis, New York, NY, 1989).

23. H. Heinz, R. A. Vaia, B. L. Farmer, R. R. Naik, Accurate Simulation of Surfaces and Interfaces of Face-Centered Cubic Metals Using 12−6 and 9−6 Lennard-Jones Potentials. *J. Phys. Chem. C* **112** (2008).
24. J.-P. Ryckaert, G. Ciccotti, H. J. C. Berendsen, Numerical integration of the Cartesian Equations of Motion of a System with Constraints: Molecular Dynamics of n-Alkanes *J. Comp. Phys.* **23** (1977).
25. J. Yin, X. Li, Z. Zhang, J. Zhou, W. Guo, Generating electricity by moving a droplet of ionic liquid along graphene. *Nature Nanotechnology* **9**, 378-383 (2014).